Significant enhancement of electrical conductivity and magnetoresistance by incorporating carbon fiber into $CoSb_3$ thermoelectric fabricated by spark plasma sintering method

Ridwone Hossain[1], Al Jumlat Ahmed[1], Sheik Md Kazi Nazrul Islam[1,2], Lina Sang[1], Frank. F. Yun[1], Guangsai Yang[1], Michael B. Cortie[2], Xiaolin Wang[1,*].

1. *Institute of Semiconducting and Electronic Materials, Australian Institute of Innovative Material, University of Wollongong, Australia.*
2. *School of Mathematical and Physical Sciences, University of Technology Sydney, Broadway, NSW 2007, Australia*

*Corresponding author: xiaolin@uow.edu.au

Abstract:

The effects of carbon fiber additions on the electrical, thermoelectric, and magnetotransport performance in *p*-type $CoSb_3$-based skutterudite are reported. A three-fold enhancement in electrical conductivity and a large increase in magnetoresistance are found. Two different explanations for the increased electrical conductivity are considered; either that carbon atoms form cause defects that makes the $CoSb_3$ more conductive, or that the increase in conductivity is due to electrical percolation of the carbon fibers in the composite. X-ray diffraction data show that the lattice parameter of the $CoSb_3$ is not affected by the presence of the carbon fiber, however adding carbon causes precipitation of 20 wt. % elemental Sb. DFT calculations show that the enthalpy of formation of a solid-solution of carbon (both interstitial and as a substitution for Sb) is favorable. These results support an explanation based on an improved electrical conductivity of a dilute solid solution of C in $CoSb_3$. The average thermoelectric parameters of the composite material, including heat conductivity, average composite Seebeck coefficient, Hall effect, carrier mobility and carrier concentration were influenced by the carbon addition. Unfortunately, the effects largely cancel each other so that the overall zT of the composite was not improved. Finally, large room temperature magnetoresistance (up to 90% at 13T) is observed, which increases with content of carbon fiber.

Keywords:

Skutterudites, carbon fiber (CF), density-of-state, electrical conductivity, figure-of-merit, composite material, thermoelectric

Introduction:

Thermoelectric materials have the excellent property of producing electricity from heat. Their availability has enabled the manufacture of thermoelectric generators which have no moving parts or working fluids, and which require negligible maintenance [1-4]. Thermoelectric technology has also expanded its use in applications such as recovering energy from waste heat from chimneys [5, 6], exhausted heat after a heat-engine produces the necessary power to drive any vehicle or generator [7-11], and conversion of abundant solar irradiance to electricity (the latter by incorporation into solar thermal or solar thermal photovoltaic systems), among other applications [12-14]. Thermoelectric materials are now widely recognized as promising energy materials, with a great deal of research and effort now focused on optimizing their physical characteristics along with finding the best candidate material for numerous energy applications.

A dimensionless figure of merit (zT) is a common benchmark for improved energy conversion efficiency of thermoelectric materials, where zT is a figure-or-merit defined by the following equation: $zT = \left(\frac{S^2\sigma}{K}\right)T$. In the above equation S, σ, k, and T are the Seebeck coefficient, electrical conductivity, thermal conductivity, and absolute temperature, respectively. In fact, power factor is essentially a function of electrical conductivity and the Seebeck coefficient (PF = $S^2\sigma$). The figure-of-merit is the determining factor for any thermoelectric material that indicates how superior the material is at some given operating temperature, with different superiority ranges for different materials. To obtain a high zT, high electrical conductivity, a high Seebeck coefficient, and low thermal conductivity are required.

$CoSb_3$-based skutterudites are one of the more promising thermoelectric materials for intermediate temperature applications, because they contain octahedral void space that can accommodate filler atoms, which could contribute to lower phonon vibrations in the lattice [15]. There have been several successful attempts to insert filler atoms into the voids of skutterudites with the intention of lowering the phonon wavelength to bring about a better zT. These atoms are known as 'rattlers' because they can move around in the void. For example, n-type $CoSb_3$ has been doped with Ga and Yb, where Ga was substituted on Sb sites while also occupying the void sites, and increasing Yb content facilitated improved Seebeck voltage and effective mass [16]. In another attempt, In (indium) was inserted into the voids of $CoSb_3$, which reduced lattice thermal conductivity without harming the power factor, whereas a slight amount of Ga substituted for Sb provided a zT of 0.9 5 [17]. In other work, several elements of group IVB were simultaneously doped into $CoSb_3$ to observe which of the elements could fill the voids, and Sn was found to be the most effective element to decrease the thermal conductivity [18]. The use of an optimum fraction of In as a fourth filler has been investigated together with the influences of microstructure, crystallite size, and thermal stability, and ways found to provide reduced thermal conductivity [19]. These types of filled $CoSb_3$ were mixed with magnetic nanoparticles at a

later stage to prepare a series of magnetic nanocomposite thermoelectric materials, where significant suppression of lattice thermal conductivity was obtained by introducing paramagnetism [20, 21].

While it is well-established that thermal conductivity in skutterites can be reduced by using filler atoms, it is important not to ignore other means by which the thermoelectric properties may be improved. If the properties can be first improved without using rattlers, then additional improvement should follow when rattlers are included later [22].

In the present work we show how a three-fold enhancement of electrical conductivity over a temperature range from 300 K to 700 K can be achieved by incorporating a small amount of carbon-fiber (CF) in *p*-type $CoSb_3$. To our knowledge, there is no published work in the literature so far that reports such a large enhancement of electrical conductivity by incorporating carbon fiber in p-type $CoSb_3$ composite. Various high electrical conductivity profiles for different proportions of carbon-fiber inclusion are demonstrated in this work. All the thermoelectric parameters were influenced by the carbon addition, although the overall zT was not significantly affected. Additionally, large magnetoresistance is observed, which increases with carbon addition.

1. Methods

1.1 Computational Details

First first-principle calculations were performed using density functional theory (DFT) implemented using the CASTEP package[23, 24]. The exchange-correlation function used to describe the exchange-correlation interaction was the General Gradient Approximation (GGA) with the Perdew–Burke–Ernzerhof (PBE) formulation [25], Structures are optimized using the Broyden–Fletcher–Goldfarb–Shanno algorithm BFGS [26]. The relevant doping is made as shown in the figures. The maximum cut-off energy was set at 420 eV with a $2 \times 2 \times 2$ k point set for optimizations with an ultrasoft pseudopotential, for the DOS the calculations were performed with a $16 \times 16 \times 16$ k point mesh. Lattice relaxation has been performed for the primitive cell for each doping case by minimizing energies to less than 5×10^{-6} eV/atom.

1.2 Sample Preparation

Finely ground $CoSb_3$ was blended with various weight percentages of carbon fiber (CF) and bulk samples prepared by spark plasma sintering (SPS) (Thermal Technology SPS Model 10 4) for 10 minutes at 500 K with 50 MPa pressure in vacuum. For comparison purposes, similar samples were prepared using graphene and graphene oxide (***suppliers here**). The $CoSb_3$ powder was purchased from Sigma-Aldrich and the purity is 99.9% based on trace metal analysis with particle size being 177 microns. The bulk samples had 20 mm diameter and 1.5 mm thickness and were subsequently cut into rectangular bars and circular discs for electronic transport measurement using a cutting machine (Struers Accutom-50). Carbon fiber additions in the $CoSb_3$ samples are denoted by different weight

percentages of carbon fiber (x=0.15, 0.35, 0.55 and 0.95 wt.%) and referred to as $CoSb_3$-CFx throughout this paper. The corresponding volume fractions of carbon (based on a carbon fiber density of 1.80 g/cm^3) are 0.63, 1.47, 2.29 and 3.91 vol.%.

1.3 Sample Characterization

Room temperature X-ray diffraction (XRD) was carried out using a Bruker D8 Discover XRD system with Cu Kα radiation. The samples were scanned in the 2θ range of 10–80° with a step of 0.02° and time per step = 1 s. The peaks due to Cu K_β were attenuated by Ni filter (D5000). Structure files for $CoSb_3$, Sb and graphite were obtained from the inorganic crystal structures database (ICSD) (https://icsd.products.fiz-karlsruhe.de/, entries 04-003-2101, 55402, and 55402 respectively) or from the Crystallographic Open Database (COD) (https://crystallography.net, entries 901-5513, 901-3415 and 900-8569 respectively). Rietveld refinement was applied using FULLPROF (www.ill.eu/sites/fullprof/ index.html) called through MATCH! (www.crystalimpact.de). The surface morphology and microstructures were observed and studied using field emission scanning electron microscopy (FE-SEM, JSM-6490LV). Energy dispersive X-ray spectroscopy (EDS) spectra were acquired with the same acquisition time, the same e-beam size and the same microscopic condition as used in obtaining SEM images. The SEM specimens were prepared after mounted in Polyfast® using Struers Citopress-20 equipment and polished with Struers Tegramin-20 water equipment. Image analysis was performed using IMAGEJ (https://imagej.nih.gov/ij/download.html). The electrical conductivity, Seebeck and power factor were measured using an Ozawa RZ2001i at room temperature to 700 K under vacuum. Carrier concentration and mobility were measured using a 13 T automated low-temperature PPMS magnet system (Quantum Design International). Low temperature resistivity was measured using the four probe method. Thermal diffusivity (D) was measured using LINSEIS LFA 1000 (Linseis Messgeraete GmbH) under vacuum conditions and, the specific heat (C_p) capacity was measured using DSC-204F1 (Netzsch GmbH) under argon atmosphere with a flow rate of 50 ml/min. The sample density (dd) was calculated using the measured weight and dimensions. The thermal conductivity (κ) was calculated by $\kappa = D \times C_p \times dd$.

2. Result and Discussion:

2.1 Electronic structure properties

Electronic structure and density of states calculations were performed using density functional theory (DFT). We first performed optimization calculations to obtain an optimized crystal structure with a lattice parameter a = 9.085 Å with the *Im-3* cubic space group (No. 204). The resulting lattice, as shown in Figure 1-(a) closely matches those of which described in Schmidt [27] with a = 9.04 Å, giving an overestimated difference of 0.5%, in agreement with previous *ab initio* calculations [28]. The enthalpy of formation was -0.21 eV/atom which is slightly more negative than the -0.1 to -0.2 eV range of experimental values reported in the literature [29] a U value of 2.5 eV was used for Co.

The results for the band structures and density of states are as shown in Figure 1(d) and 1(e). As we can see, they closely match those described in Yang [30]. Band structure calculation results using the primitive cell shown in Figure 1(b) of the pure $CoSb_3$ structure with the K-path in the Brillion zone of $\Gamma \rightarrow H \rightarrow N \rightarrow P \rightarrow \Gamma \rightarrow N$ (Figure 1(c)) show the characteristics of a small gap semiconductor. The semiconductor has an direct band gap of 0.224 eV that matches previously reported value by Sofo [31]. Figure 1(e) shows the contributions of carriers from *s, p* and *d* orbitals with the major contributor of the highest occupied molecular orbital (HOMO) being the *p* and *d* orbital electrons. The origin of these *p* and *d* orbitals are recognized from the Sb and Co ions respectively. Although Sb *p* vs Co *d* overall contribution are similar, it must be noted that there is 3 vs 1 population ratio and, as such, per atom the Co *d* orbital contribution to the HOMO is much higher.

Previous studies have concluded that $CoSb_3$ can be doped to become either *n* or *p*-type [32, 33] depending on whether electron or hole dopants are used. Three scenarios have been taken into account for our calculations to simulate the possible impact of carbon in the $CoSb_3$ lattice. These include the replacement of either the Sb or Co ions with carbon atoms within the primitive $CoSb_3$ crystal structure (to simulate the substitutional states), the removal of the Co or Sb ions from within the crystal structure (to simulate defect states), and finally the insertion of one, two and three carbons within the crystal structure (to simulate the interstitial states).

In our calculated results, we observe that in the C-Co substitutional state (Figure 2(a-b)) there is a slight peak in the HOMO from the *s* orbital contributions from the carbon atom and hence there is a similar contribution to the Fermi level between the *s* vs *d* orbitals. Surprisingly there is an overall increase in the *p* and *d* orbital contributions which is likely due to the result of the delocalization of the *p* orbitals from the *d* orbitals of the Co ions although it of interest to note that *d* orbitals are also delocalized. This delocalization of *d* orbitals is likely attributed to the broken symmetry between the Sb and Co ions where *d* orbitals are partially delocalized from the Co. In the Sb substitutional state (Figure 2(c-d)), we

observe that there is a similar increase in the *p* and *d* orbital contributions although there is no *s* orbital HOMO peak. As such, the contribution to the Fermi level for *d* orbitals is much greater than the *s* orbital, but similarly, because of the broken symmetry, there is also a delocalization of the *p* orbitals from the Sb. However, in all cases, there is an overall increase in the total contribution at the Fermi energy.

The calculated enthalpies of formation for the various configurations are listed in Table 1. Note that the formation of an interstitial solid solution of carbon in certain sites is favorable and so is the substitution of Sb with a carbon. Substitution of a Co with a carbon is not favorable.

Atoms are removed from the position as shown in Figure 3(c) for Co and Figure 3(d) for Sb. In both the Co defect states (Figure 3(a)), there is a higher *p* orbital contribution for HOMO orbitals, due to the fact that *p* orbitals were previously localized by Co in the pure $CoSb_3$. Hence, further enhancement of *p* orbital contributions can be observed since Sb *d* orbitals do not contribute to HOMO orbitals. In the Sb defect state, this is reversed and there is a comparatively higher *d* orbital HOMO contribution observed because of the delocalized *d* orbitals which were previously localized in pure $CoSb_3$. The lowering of *p* orbital is expected since the majority of the contribution comes from Sb. The changes in the orbitals are consistent with *p*-*d* hybridization between the *p* orbital of the Sb and *d* orbitals of the Co. In both cases, there is an overall increase in total contribution at the Fermi energy. However, the defect doping states show a *p*-type conduction of electrons.

The interstitial carbon states show an overall increase in the *p* orbital contribution of the HOMO which is due to the carbon *p* orbital contributions. This carbon *p* orbital contribution is in addition to the Sb *p*-orbital contributions to the HOMO (Figure 4(c)). Up to three carbon atoms are inserted into the lattice at three different positions in Figure 4(a) where these are indicated as C1, C2 and C3, (the numerals indicate the total number of carbon atoms). Our results show that the *p* orbital contribution increases with an increasing amount of carbon atoms (Figure 4(b-d)), but as the number of carbon atoms increases the contribution, per carbon atom is decreasing (Figure 5-(a)) . However, all interstitially- doped orbitals show hole-like properties in their density of states (Figure 4(b-d)). Finally placing a carbon atom in a 'rattler' site is unfavorable. Similar trends emerge for all three cases interstitial, substitutional and defect doping all increase the total density of states at the fermi energy which can explain why there is a overall increase in the conductivity as all forms of defect will contribute to the overall increase in conductivity.

It is worth noting that the relaxed lattice parameters of the carbon-containing structures is slightly bigger than the starting structure. Based on this evidence we would expect a change of 0.5% in the experimentally determined lattice parameters of the carbon-containing samples.

Table 1. Enthalpies of formation and relaxed lattice parameters from the DFT calculations. These calculations were performed with CASTEP. and began with P1 symmetry on the primitive cell of the $CoSb_3$ structure. Enthalpies of formation are relative to the pure solid elements in their standard crystalline state at 0 K. The calculated enthalpy of formation of pure $CoSb_3$ matches the range reported from experiments (-0.09 to -0.16 eV per atom [29]).

Phase	Description	ΔH, eV/atom	a_0, Å
Co_8Sb_{24}	standard state	-0.09/-0.21	7.87
Co_8Sb_{23}	Sb deficient	+0.01/-0.05	7.82
Co_7Sb_{24}	Co deficient	-0.08/-0.084	7.87
$Co_7Sb_{24}C$	C on Co site	+0.31/0.18	7.96
$Co_8Sb_{23}C$	C on Sb site	-0.30/0.04	7.78
$Co_8Sb_{24}C$	interstitial C at (0,½,½)	-0.38/0.05	7.91
$Co_8Sb_{24}C_3$	interstitial C at (0,0,0)	0.18	7.89
$Co_8Sb_{24}C_3$	interstitial C at (0,½,½), (½, 0,½) & (½,½,0)	+0.12/0.52	8.00

We next look at the measured effects of carbon addition on the structure, electrical, thermoelectric and magnetoresistance properties of $CoSb_3$.

2.2 Structural and morphology characterization

The powder XRD patterns (Figure 6) of all the samples indicate that the major peaks are from the polycrystalline skutterudite structure of $CoSb_3$. There are also peaks for Sb in all of the samples to which CF was added. In some cases a 002 graphite peak was also evident. Note however that the small amount (<1 wt.%) of carbon deliberately added would not be detectable by XRD under the present conditions even if all of it was perfectly graphitized (an observation also made by Feng et al.[22]). We concluded, like Liu et al. [34] did, that the peak for graphite in samples made by SPS was spurious and due to residual graphite foil being present from the SPS synthesis. The results of the Rietveld analyses are provided in Table 2 (the region containing the spurious 002 graphite peak was masked off in these refinements). It is clear that (i) including CF up to 0.95 wt.% does not cause any significant change in lattice parameters of the $CoSb_3$ and (ii) the CF-containing samples contained a consistent 20 ± 2 wt.% elemental Sb as a second phase.

Table 2. Results of Rietveld refinement on a mixed $CoSb_3$ plus Sb microstructures.

Wt.% carbon added as carbon fiber	Lattice parameter for $CoSb_3$	Wt.% of Sb on surface from Rietveld analysis	Weighted Bragg R factor	χ^2
0.00	9.0355 ± 0.0008	0	12.6	4.3
0.15	9.0363 ± 0.0005	22.5 ± 0.3	12.3	5.5
0.35	9.0363 ± 0.0005	18.1 ± 0.3	11.2	4.6
0.55	9.0356 ± 0.0003	20.1 ± 0.3	14.4	5.5
0.95	9.0361 ± 0.0003	20.4 ± 0.2	11.4	5.1

Figure 7 shows SEM micrographs of polished sample surfaces (Figure 7(a-c)) and cross-section morphology (Figure 7(d-f)) for the $CoSb_3$ polycrystalline samples with and without carbon fiber addition. The carbon fibers become quite prominent as the carbon concentration increases from x=0.15 to 0.95 wt.%. The predicted volume fraction of carbon fiber in the 0.55 and 0.95 wt.% C samples is 2.3% and 3.9% respectively (based on a CF density of 1.80 g/cm^3) while image analysis of the respective polished sections indicated values between 2 and 4%. Figure 8 shows EDS mapping of the samples and confirms the presence of the CF but not if second phase Sb. We speculate that the Sb precipitates are below the resolution of the map. Raman measurements showed that the CF was slightly more graphitic after incorporation into the $CoSb_3$ matrix, Figure 9. The experimental volume fractions and Raman spectra indicates that most of the CF passes unchanged through the SPS process.

All the samples are found to be densely aggregated, with little porosity. This is due to the relatively high temperature and pressure, and long times, used in the SPS processing. The grain sizes are about 5 μm or less. Energy dispersive spectroscopy (EDS) performed on the x=0.55 wt.% C sample is presented in Figure 10 and confirms the identity of the microstructural constituents. By using the reported errors in the EDS, the ratio of Sb:Co was estimated to be in the range to 2.85 to 3.21, i.e. the sample should be mostly $CoSb_3$. The Sb precipitates found by the XRD were too small to be readily visible at the magnification used for SEM EDS mapping.

2.3 Electrical and thermal properties:

In Figure 11, electrical conductivity *vs.* temperature is shown for different samples over a range of temperatures. The electrical conductivity increases by a factor of about three with increasing carbon fiber addition up to 0.35 wt.% C but the effect saturates for greater additions. For the pure $CoSb_3$, the electrical conductivity rose from 271 S.cm^{-1} at 330 K to 355 S.cm^{-1} between 300 and 700 K whereas the highest value ($CoSb_3$-CF0.35) reaches 1189 S.cm^{-1} at 330 K and goes down to 973 S.cm^{-1} at 700 K.

Importantly however, the trends depicted for pure $CoSb_3$ (x=0) and the $CoSb_3$-CFx are qualitatively different: while monotonic increase is observed in pure $CoSb_3$ from room temperature to 700 K, a noticeable drop occurs for the $CoSb_3$-CFx composites. These facts have important implications – the pure $CoSb_3$ is behaving as semiconductor (as it should) but the $CoSb_3$-CFx composites are performing with a degree of metal-like behavior.

The enhancement of electrical conductivity in the $CoSb_3$-CFx composites is accompanied by a significant reduction in Seebeck coefficient, Figure 11(d). For example, the Seebeck value is only 65 μVK^{-1} for $CoSb_3$-CF0.35 at 700 K as compared to 163 μVK^{-1} at 700 K for pure $CoSb_3$. All the samples remain *p*-type, as expected from their content of elemental Sb [34].

Power factor (PF) = $S^2\sigma$ has been represented in Figure 12 as a function of temperature for $CoSb_3$-CFx composites and compared with pure $CoSb_3$. While carbon fiber additions significantly increased electrical conductivity, the Seebeck coefficients dropped below that of pure $CoSb_3$. Since Seebeck values are squared and multiplied with σ to obtain power factor, it can be appreciated that Seebeck values dominate over σ. For this reason, all the samples showed reduced power factor as compared to pure $CoSb_3$.

Thermal diffusivity (TD), specific heat capacity (C_p), density (ρ) are the basic thermal property components which may be combined via k=TD×C_p×ρ to yield thermal conductivity (k). The thermal conductivity arises from two contributions, the electronic thermal conductivity (K_e) and the phonon thermal conductivity (K_{ph}), therefore, total thermal conductivity is $K = K_e + K_{ph}$ [12]. It should be noted that the overall thermal conductivity is dominated numerically by phonon thermal conductivity which means that phonon vibration in the lattice contributes to heat propagation more than electronic heat propagation at high temperature.

Measured thermal conductivity for the $CoSb_3$-CFx samples is shown in Figure 13 as a function of temperature. The carrier component k_c (Figure 13(b)) has been estimated using the Wiedermann-Franz Law (K_e=L.σ.T, where L is a constant known as the Lorenz number [35]) and phonon thermal conductivity k_{ph} (Figure 13(c)) found by difference. In this work, L is calculated according to the equation $L = 1.5 + \exp[-|S|/116]$, where L is in $10^{-8}\ W\Omega \cdot K^{-2}$ and S in $\mu V \cdot K^{-1}$[36, 37]. The calculated results show that L varies in the range of $(1.7 - 2.2) \times 10^{-8}\ W\Omega \cdot K^{-2}$ with different types of CF addition and with the temperature increasing from 330 to 700 K. The $CoSb_3$-CFx samples show

increased carrier thermal conductivity over a wide range of temperature in Figure 13(b) as amount of carbon fiber added is increased.

K_{ph} is also observed to be increasing with carbon fiber addition (Figure 13(c)) which could be due to the presence of carbon fiber in between the grain boundaries acting as a bridge between crystal boundaries and thereby helping phonons to travel from one grain to another. Actually, since thermal conductivity of carbon fiber can be much greater (up to as high as 180 $W.m^{-1}.K^{-1}$ [38] depending on degree of graphitization) than that of the pure $CoSb_3$, (~8 $W.m^{-1}.K^{-1}$ at room temperature), some increase in the overall value of *k* for an engineering composite made of the two substances is not unexpected. In contrast, some previous experiments have shown that carbon fiber or graphene in between grains can *reduce* the lattice thermal conductivity due to lattice mismatch between grain and carbonaceous second phase, both in $CoSb_3$ [39] and Cu_2Se [40, 41]. We will return to this difference in behavior in the Discussion.

2.4 Magnetotransport and Hall effect measurements

To further investigate the influence of carbon fiber addition on the transport properties of $CoSb_3$, we have measured the magnetoresistance (MR) and Hall effect of $CoSb_3$-CF*x* samples at 300 K as shown in Figure 14. The transverse MR, defined as $100\% * [\rho(B) - \rho(0)]/\rho(0)$, where ρ is the resistivity and B is the magnetic field shows a classic B^2 trend at low field for all samples and then the MR increases with magnetic field in a more linear relation in the high-field region. Essentially, both the Hall effect coefficient and the magnetoresistance are being measured for a microstructural composite of $CoSb_3$, Sb and CF and it is not a simple matter to extract the values for the individual phases [42]. As such, the values reported here can be considered to be those of an 'effective medium' representing the composite. The Hall coefficient is given by $R_H = \rho_{xy}/B$, where B is the magnetic flux density, ρ_{xy} is the Hall resistivity. The carrier concentration is $p = -1/(R_H e)$, where e is the electron charge. For all carbon concentrations, the values of R_H are positive indicating dominant *p*-type conduction (as indeed expected from the positive Seebeck coefficients). It can also be observed that the carrier concentration increases significantly with CF addition. Figure 11(b) shows the effect of carbon content on the in-plane conductivity and Hall mobility at 300 and 340 K, respectively. The Hall mobility follows the formula $\mu_H = R_H * \sigma$; σ is the in-plane conductivity. Compared to pure $CoSb_3$ sample, the mobility decreases sharply with the initial addition of carbon. Further increase in carbon concentration results in a slight increment with minimal rate of change after x=0.35 wt.%.

4. Discussion

4.1 Origin of enhanced electrical and thermal conductivity

Although the percolation of randomly packed conductive spheres occurs at a volume fraction of about 18% [43], it is a surprising fact that percolation of random dispersions of conducting fibers, or other reinforcements with very long aspect ratio, can occur in composite materials at as low as 0.5 vol.% [44-46]. The mechanism of conduction in such composites includes both direct electrical pathways and a network of tunnel junctions. This low threshold is well within the range of volume fractions of carbon fiber investigated in the present work, however typical values for the electrical conductivity of industrial carbon fibers are of the order 20 to 2000 $S.cm^{-1}$ and 10 to 180 $W.m^{-1}.K^{-1}$ respectively. The spread is probably due to a variable degree of graphitization. This is similar order to the intrinsic properties of the $CoSb_3$ matrix anyway so percolation of CF is not likely to change the composite conductivity much (or at all). Rather, it is more likely that the changes in the present series of sample are due to a change in the electronic characteristics of the matrix.

4.2 Increased thermal conductivity

As mentioned earlier, the thermal conductivity in an electrically conductive solid may be broken into electronic and vibrational components. In the present composite system, high electrical conductivity is ensured by some change in the carrier characteristics due to carbon doping. This factor in turn provides a strong contribution to k_c. Scattering of phonons off carbonaceous inclusions, which has provided quite a reliable reduction of k_{ph} in other systems, including $CoSb_3$/graphene[39] and Cu_2Se/carbon[41], is simply overwhelmed in the present case by the electronic contribution to k. The overall result is that zT in this system is not improved by the CF additions, Figure 15.

5. Conclusion

We have demonstrated a new approach for the fabrication of *p*-type $CoSb_3$-based composite material whereby carbon fiber has been incorporated by the SPS method. The thermoelectric, electronic and magnetoresistance properties were investigated for carbon fiber contents of up to 0.55 wt.% (corresponding to 2.3 vol.% C). A three-fold improvement in electrical conductivity over that of pure $CoSb_3$ was obtained when x=0.35 wt.%C This corresponds to ~1.5 vol.% carbon fiber. Additions of carbon fiber greater than this were not more beneficial. We suggest that, under the specific processing conditions used, a saturated solid solution of carbon in the $CoSb_3$ lattice forms when CF is added to the starting mixture at about 1.5 vol.%. Larger amounts do not contribute more to electrical conductivity. Thermal conductivity is slightly raised by the additional of carbon fiber. This illustrates that heat conduction in this system is dominated by electronic effects and that any increased scattering of phonons by the carbon fibers only has a secondary effect on thermal conductivity in these samples. Future work

on this system must therefore necessarily concentrate on lowering thermal conductivity in order to restore the zT values, for example by including 'rattler' atoms within the $CoSb_3$ lattice to reduce thermal conductivity.

Competing interest

We declare that we have no competing interests.

Acknowledgement

Higher degree research of Ridwone Hossain was partially supported by a university faculty scholarship. This work was partially supported by the Australian Research Council (ARC) through Discovery Projects DP 130102956 (X.W.), DP 180100645 (M.C.), an ARC Professorial Future Fellowship project (FT 130100778, X.W.) and a Linkage Infrastructure Equipment and Facilities (LIEF) grant (LE 120100069, X.W.). The authors also acknowledge the use of the JEOL JSM 6490LV SEM funded by the Australian Research Council (ARC) – Linkage, Infrastructure, Equipment and Facilities (LIEF) located at the UOW Electron Microscopy Centre.

Reference:

[1] DJEC Champier, Management (2017) 140: 167.
[2] D Zhao, GJATE Tan (2014) 66: 15.
[3] MH Elsheikh, DA Shnawah, MFM Sabri, et al. (2014) 30: 337.
[4] W Liu, Q Jie, HS Kim, ZJAM Ren (2015) 87: 357.
[5] Y Miyazaki, Y Saito, K Hayashi, K Yubuta, TJJJoAP Kajitani (2011) 50: 035804.
[6] AE Özdemir, Y Köysal, E Özbaş, TJEC Atalay, Management (2015) 98: 127.
[7] Y Wang, C Dai, SJAE Wang (2013) 112: 1171.
[8] N Espinosa, M Lazard, L Aixala, HJJoEm Scherrer (2010) 39: 1446.
[9] EJ Carlson, K Strunz, BP Otis (2010) Solid-State Circuits, IEEE Journal of 45: 741.
[10] V Dolz, R Novella, A García, JJATE Sánchez (2012) 36: 269.
[11] R Saidur, M Rezaei, WK Muzammil, et al. (2012) 16: 5649.
[12] GJ Snyder, ES Toberer (2008) Nature Materials 7: 105. Doi:10.1038/nmat2090
[13] MS Dresselhaus, G Chen, MY Tang, et al. (2007) Advanced materials 19: 1043.
[14] JR Sootsman, DY Chung, MG Kanatzidis (2009) Angewandte Chemie International Edition 48: 8616.
[15] M Rull-Bravo, A Moure, J Fernandez, M Martin-Gonzalez (2015) Rsc Advances 5: 41653.
[16] X Shi, J Yang, L Wu, et al. (2015) Scientific Reports 5: 14641. Doi:10.1038/srep14641

https://www.nature.com/articles/srep14641#supplementary-information

[17] KK Seongho Choi1, Adul Harnwunggmoung2, Yoshinobu Miyazaki1, Yuji Ohishi1, Hiroaki Muta1 and Shinsuke Yamanaka1,3 (2015) Japanese Journal of Applied Physics Volume 54, Number 11.
[18] W-S Liu, B-P Zhang, L-D Zhao, J-F Li (2008) Chemistry of Materials 20: 7526. Doi:10.1021/cm802367f
[19] G Rogl, A Grytsiv, K Yubuta, et al. (2015) Acta Materialia 95: 201. Doi:https://doi.org/10.1016/j.actamat.2015.05.024
[20] W Zhao, Z Liu, P Wei, et al. (2017) Nature nanotechnology 12: 55.
[21] W Zhao, Z Liu, Z Sun, et al. (2017) Nature 549: 247.
[22] B Feng, J Xie, G Cao, T Zhua, X Zhao (2013) J. Mater. Chem. A 1: 13111.
[23] J Clark Stewart, D Segall Matthew, J Pickard Chris, et al. (2005) Zeitschrift für Kristallographie - Crystalline Materials,
[24] SJ Clark, MD Segall, CJ Pickard, et al. (2005) 220: 567.
[25] JP Perdew, K Burke, M Ernzerhof (1996) Physical Review Letters 77: 3865. Doi:10.1103/PhysRevLett.77.3865
[26] DF Shanno (1970) Mathematics of Computation 24: 647. Doi:10.2307/2004840
[27] T Schmidt, G Kliche, H Lutz (1987) Acta Crystallographica Section C: Crystal Structure Communications 43: 1678.
[28] R Guo, X Wang, B Huang (2015) Scientific reports 5: 7806.
[29] ME Schlesinger (2013) Chem. Rev. 113: 8066−8092. Doi:dx.doi.org/10.1021/cr400050e
[30] J Yang, L Zhang, Y Liu, et al. (2013) Journal of Applied Physics 113: 113703.
[31] JO Sofo, GJPRB Mahan (1998) 58: 15620.
[32] X Shi, J Yang, JR Salvador, et al. (2011) Journal of the American Chemical Society 133: 7837.
[33] G Rogl, A Grytsiv, P Rogl, et al. (2010) Intermetallics 18: 2435.
[34] W-S Liu, B-P Zhang, J-F Li, L-D Zhao (2007) J. Phys. D: Appl. Phys. 40: 6784. Doi:doi:10.1088/0022-3727/40/21/044
[35] NW Ashcroft, ND Mermin (1976) Solid State Physics. Harcourt College Publishers, , New York
[36] H-S Kim, ZM Gibbs, Y Tang, H Wang, GJ Snyder (2015) APL materials 3: 041506.
[37] RJ Mehta, Y Zhang, C Karthik, et al. (2012) Nature materials 11: 233.
[38] Y El-Hage, S Hind, F Robitaille (2018) J. Textiles Fibrous Mater. 1: 1.
[39] P-a Zong, R Hanus, M Dyll, et al. (2017) Energy Environ. Sci. 10: 183.
[40] SMKN Islam, MB Cortie, X Wang (2020) J. Mater. Chem. A: in press.
[41] M Li, DL Cortie, J Liu, et al. (2018) Nano Energy 53: 993.
[42] TW Day, WG Zeier, DR Brown, BC Melot, GJ Snyder (2014) Appl. Phys. Lett. 105: 172103.
[43] MJ Powell (1979) Phys. Rev. B 20: 4194.
[44] K Miyasaka, K Watanabe, E Jojima, H Aida, Masao Sumita, K Ishikawa (1982) J. Mater. Sci. 17: 1610.
[45] M Haghgoo, R Ansari, MK Hassanzadeh-Aghdam, M Nankali (2019) Composites Part A 126: 105616.
[46] A Motaghi, A Hrymak, GH Motlagh (2015) J. Appl. Polymer Sci. 2015, : 41744. Doi:DOI: 10.1002/APP.41744

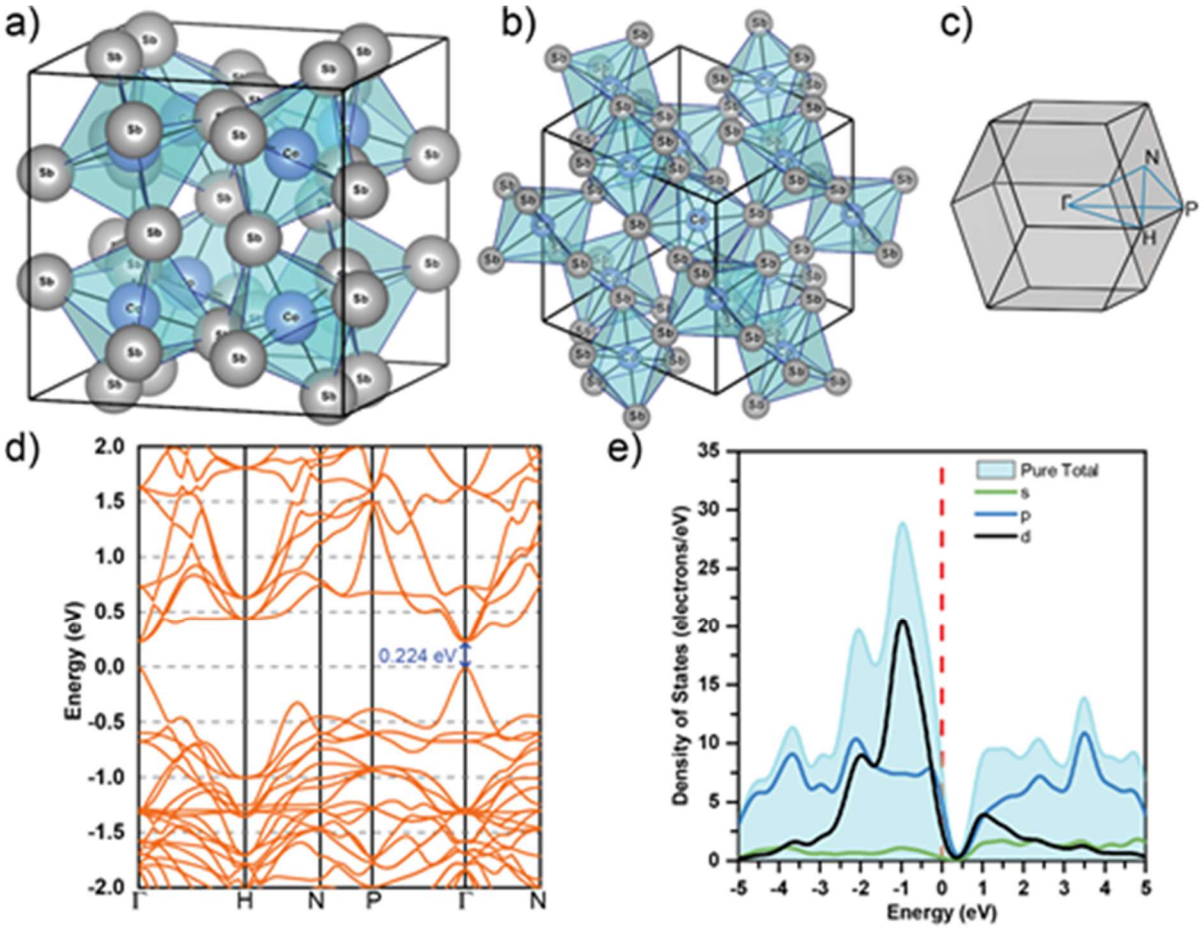

Fig 1 (a) Crystal structure of $CoSb_3$ unit cell (b) primitive cell (c) Brillouin zone of the primitive cell (d) first-principles band structure calculation of pure $CoSb_3$ where the zero-energy point represents the Fermi level (e) contributions of electrons from different orbitals

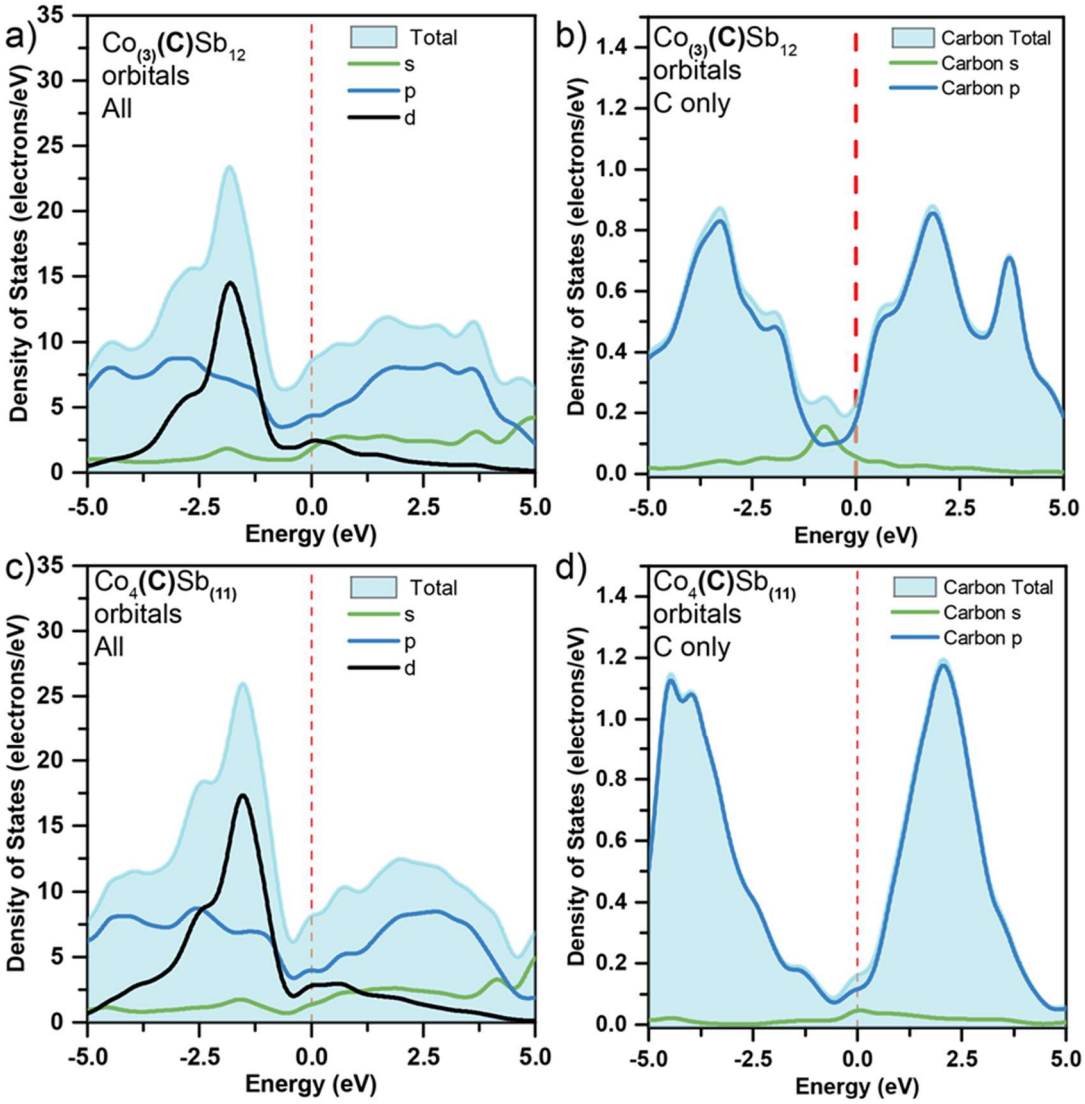

Fig 2 Partial density of states for doped $CoSb_3$ in which carbon substitutionally dopes Co (a) and Sb (c) and the respective (b & d) partial density of states for their carbon contribution

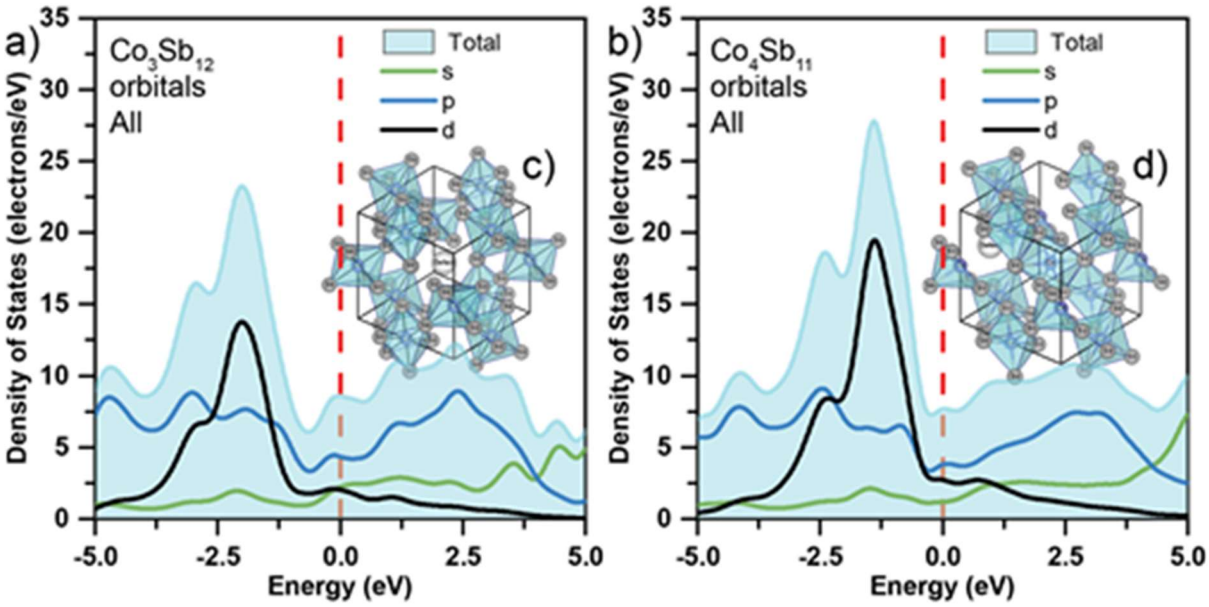

Fig 3 Density of states for defects state (voids) doped $CoSb_3$ in which a void exists in the Co (a & c) and Sb (b & d) position

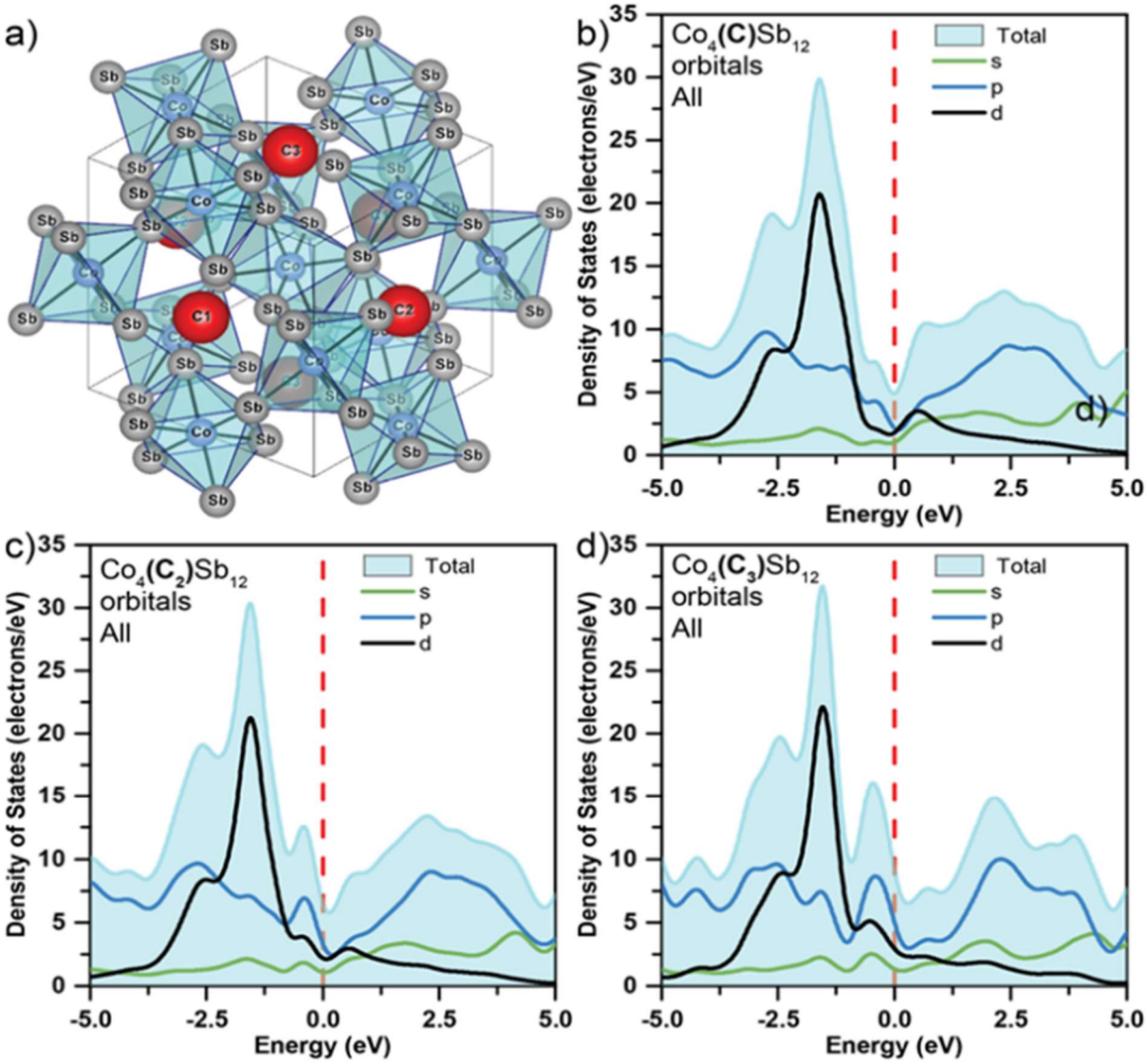

Fig 4 C1 C2 C3 in (a) shows the positions of the interstitial carbon doping. Density of states of interstitially doped $CoSb_3$ for (b) C1 (c) C2 and (d) C3 carbon ions

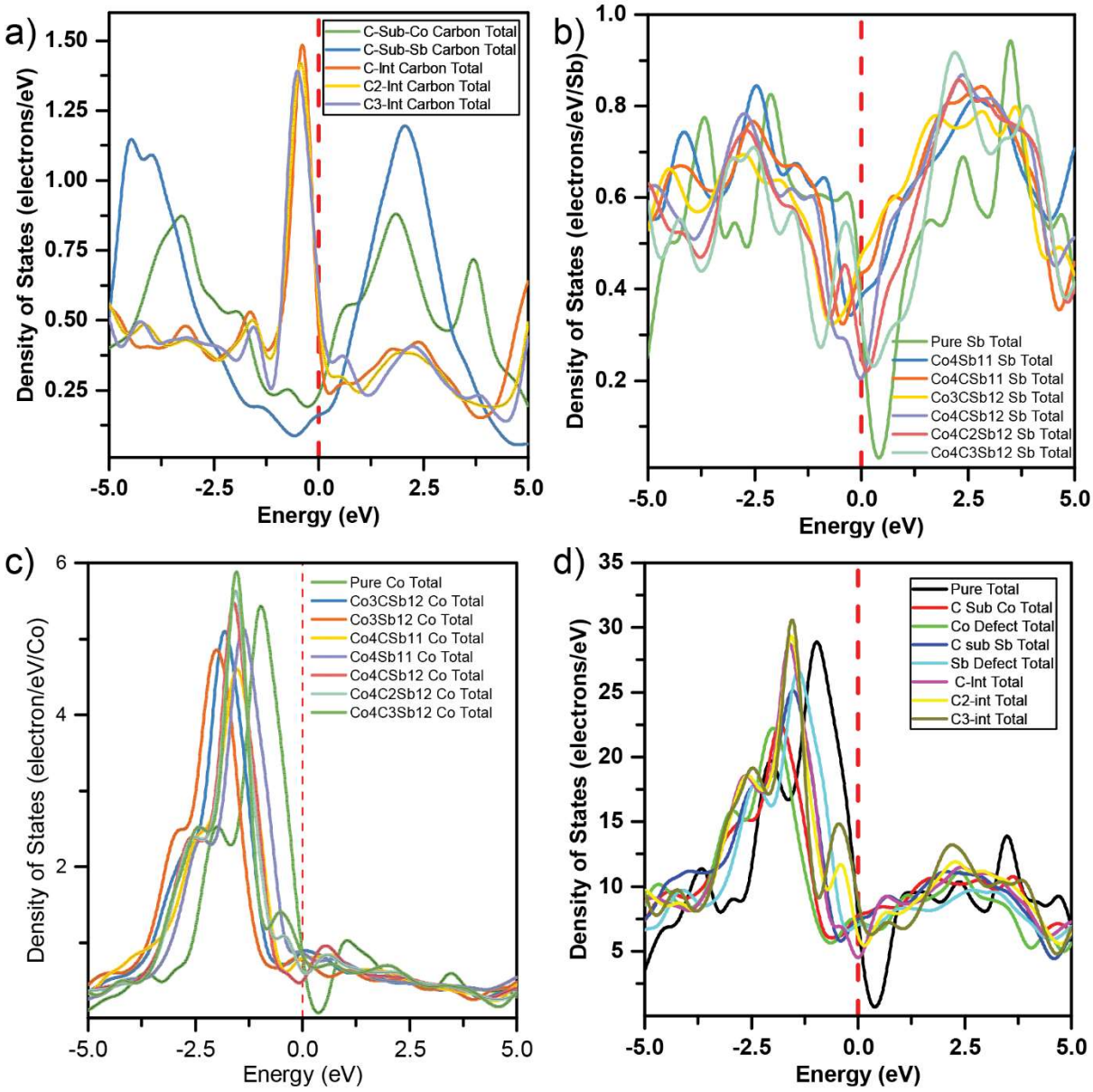

Fig 5 Comparison of all doping scenarios changes in (a) carbon (b) Sb (c) Co per each atom and (d) their respective totals

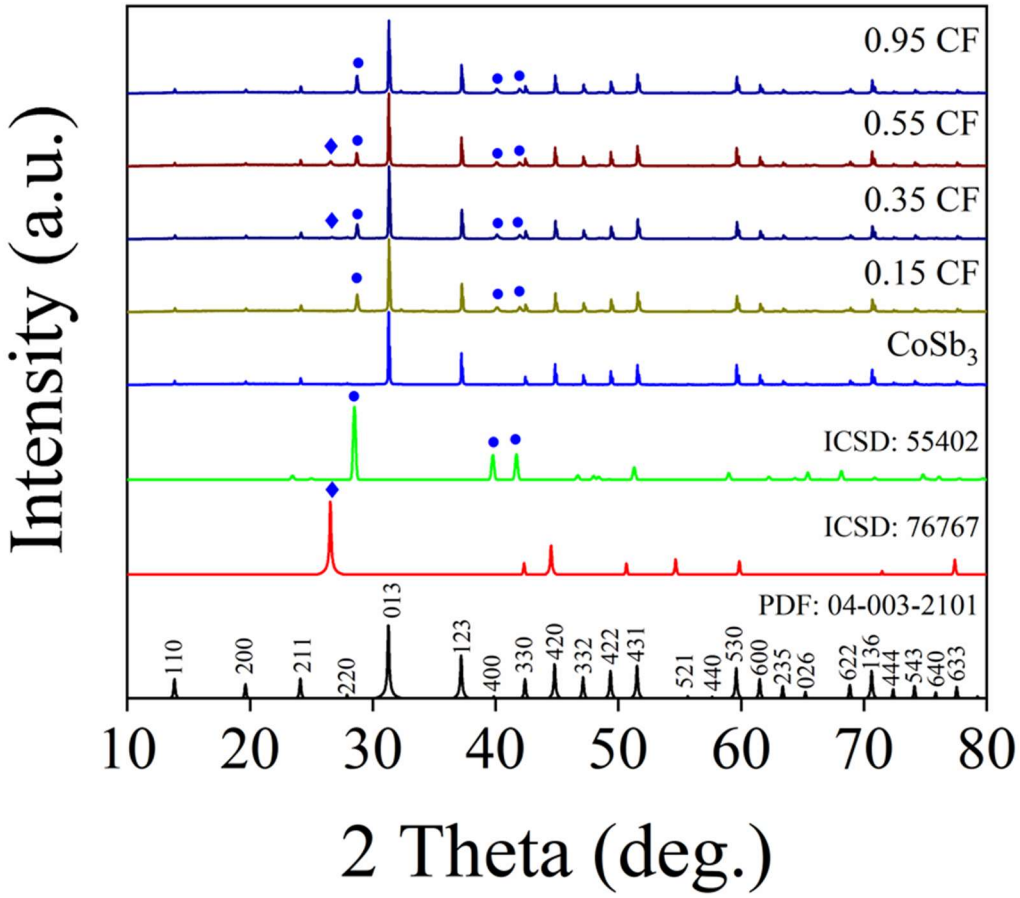

Fig 6 Room temperature X-ray diffraction patterns of the samples match with $CoSb_3$ (PDF number 04-003-2101), hexagonal structured carbon (ICSD collection code 76767) and, in the samples with carbon fiber, trigonal structured antimony (ICSD collection code 55402). $CoSb_3$ samples with a content of carbon fiber are named as $CoSb_3$-*x* wt% CF (*x* =0, 0.15, 0.35, 0.55 and 0.95 wt.% carbon fiber)

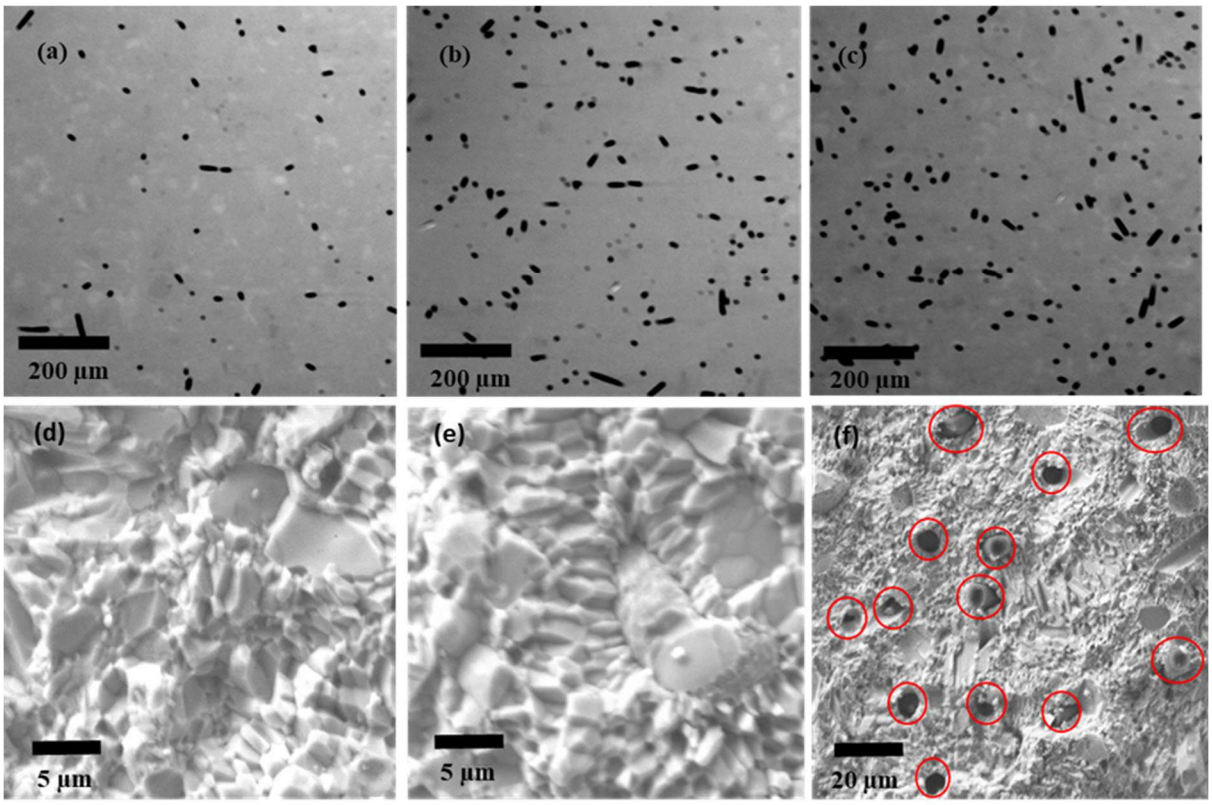

Fig 7 SE-SEM image of surface and cross-sectional morphology of $CoSb_3$ samples with nominal compositions of $CoSb_3$-CF_x (a & d) x=0.15 wt.% (b & e) x=0.35 wt.% and (c & f) x=0.55 wt.%. Black dots in panels a, b and c are carbon fibre on the surface. Red circles in panel (f) indicate carbon fibres found in the cross-section.

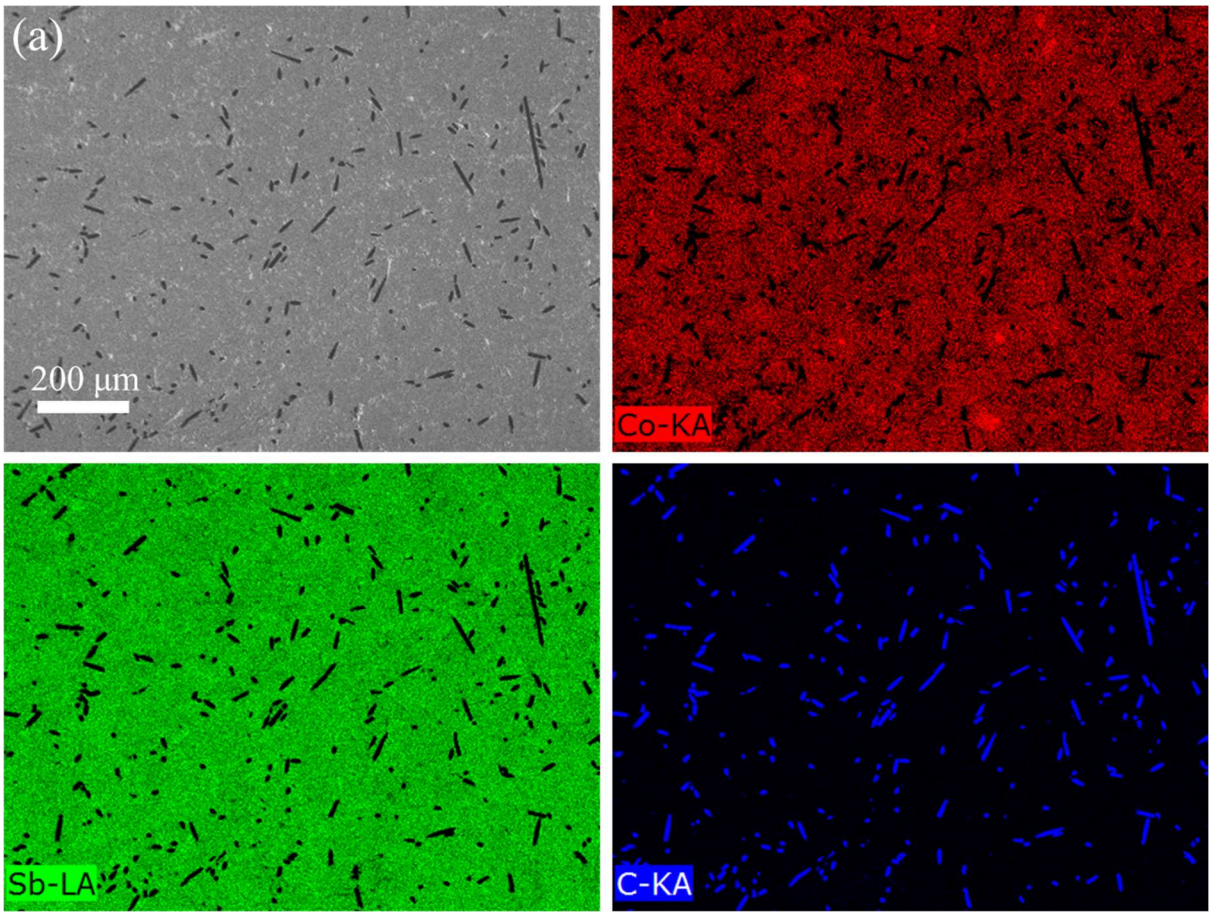

Fig 8 SE-SEM image of the polished 0.95wt.% CF incorporated $CoSb_3$ sample, showing CF rich precipitates within the $CoSb_3$-rich matrix along with the corresponding EDS elemental mapping for Co, Sb and C.

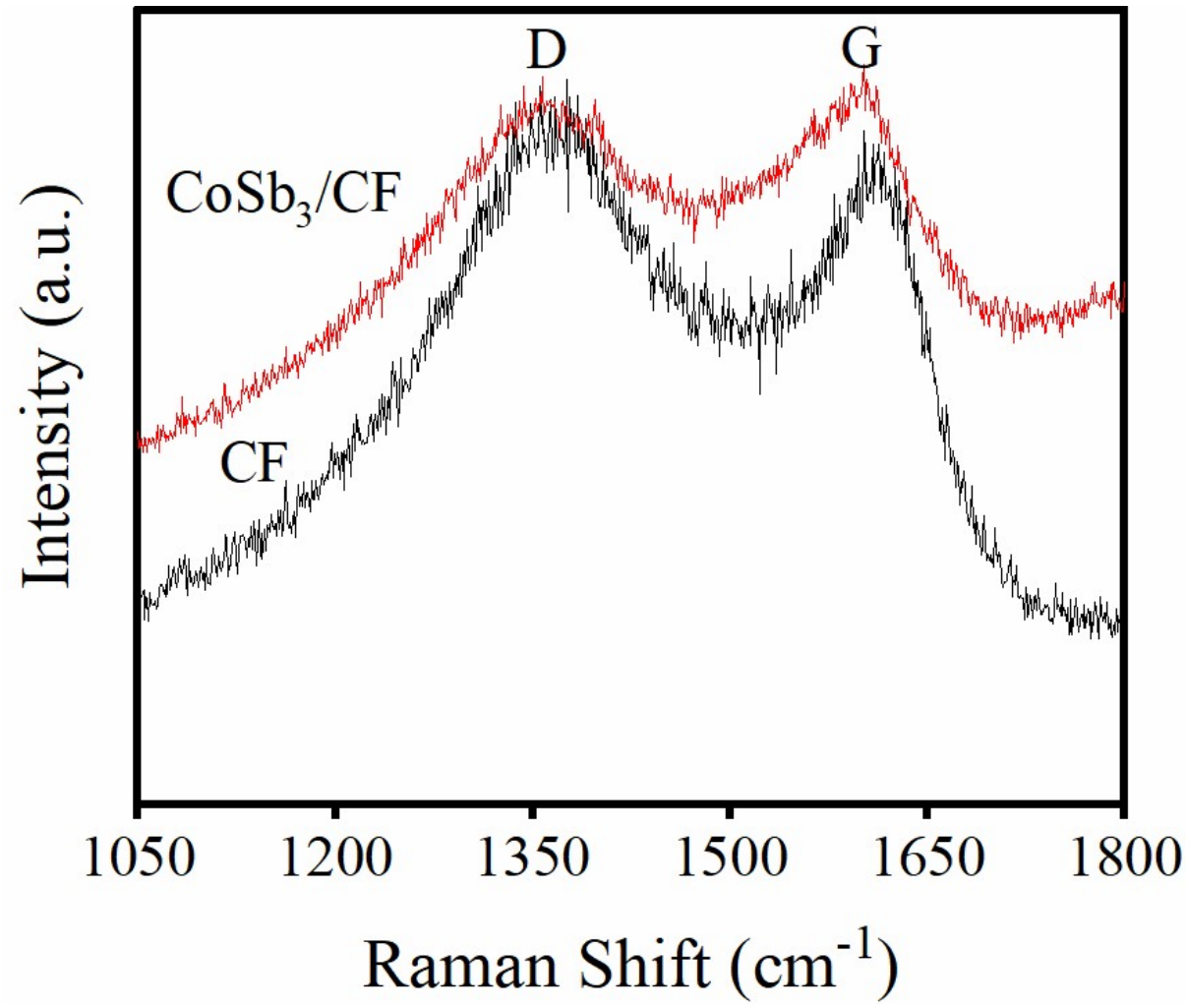

Fig 9 Raman spectra for carbon fiber before and after incorporation into sample.

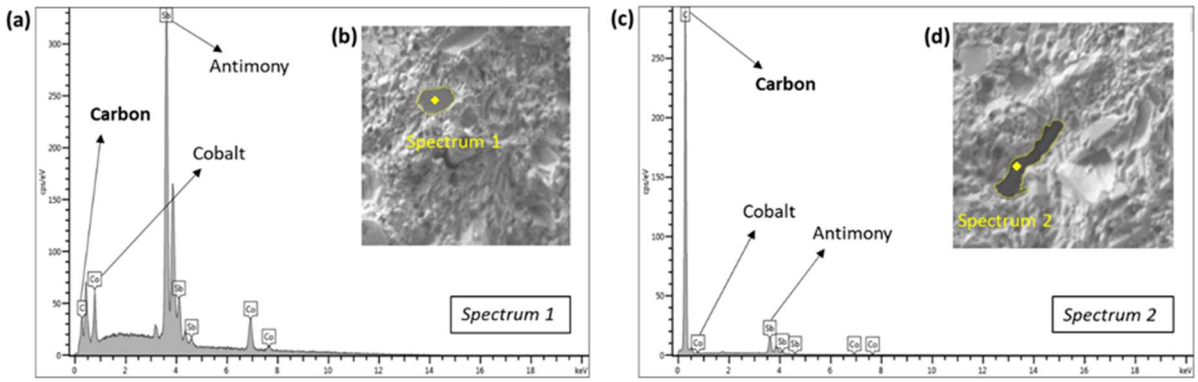

Fig 10 (a) Energy-dispersive X-ray spectroscopy (EDS) spectrum of the selected region of panel (b) and (c) EDS spectrum of selected region of panel (d). Both the figures in (b) and (d) are $CoSb_3$-CF0.55 wt.%.

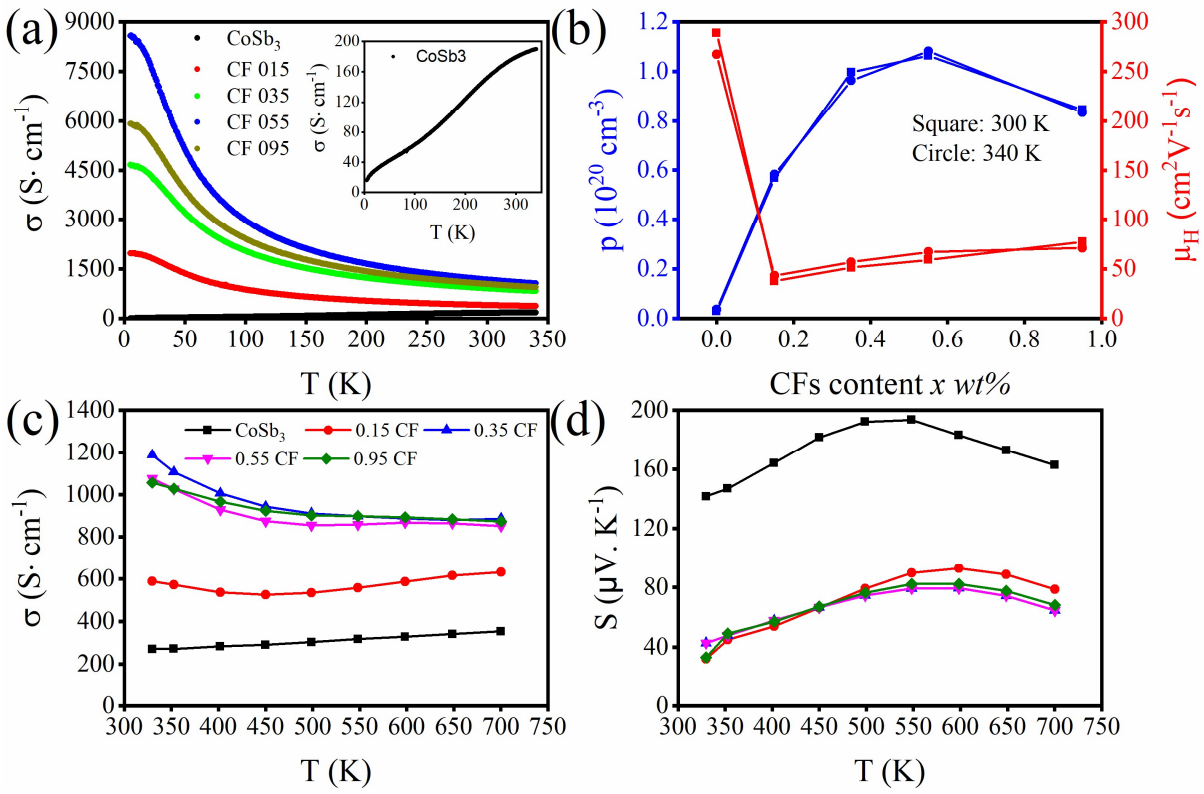

Fig 11 Temperature dependence of electrical transport properties of pure $CoSb_3$ and CF incorporated $CoSb_3$ samples ($CoSb_3$-xwt% CF (x =0, 0.15, 0.35, 0.55 and 0.95wt.% carbon fiber). (a) low temperature electrical conductivity (σ), (b) Carrier concentration and carrier mobility, (c) high temperature electrical conductivity (σ), (d) Seebeck coefficient (S) as a function of temperature.

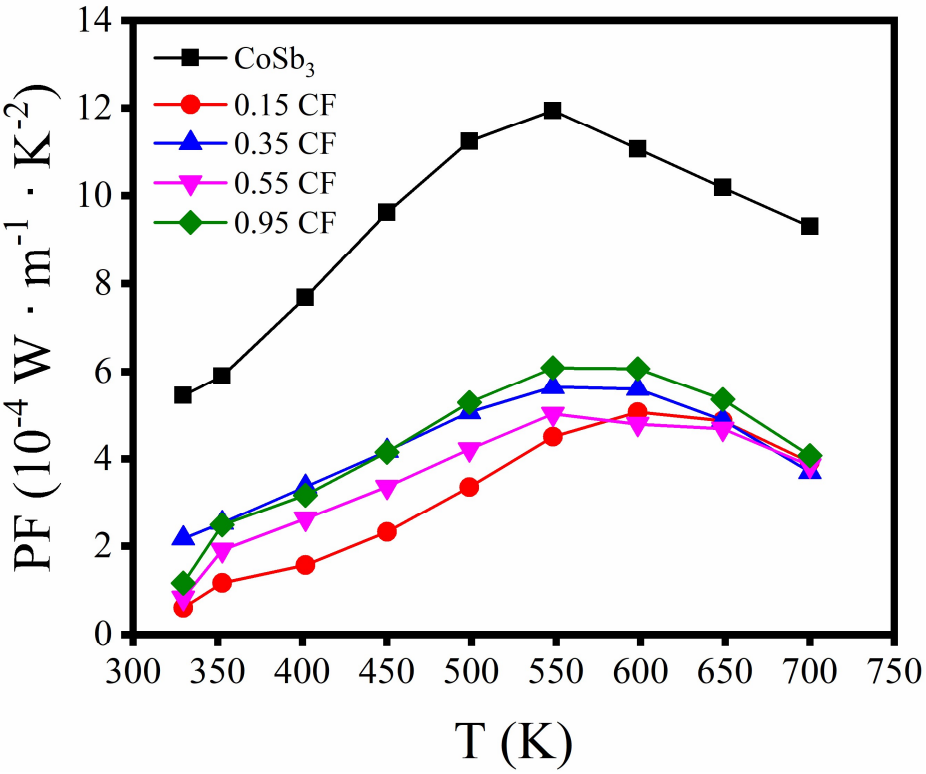

Fig 12 Temperature dependence of power factor of pure $CoSb_3$ and CF incorporated $CoSb_3$ samples ($CoSb_3$-xwt% CF (x =0, 0.15, 0.35, 0.55 and 0.95wt.% carbon fiber).

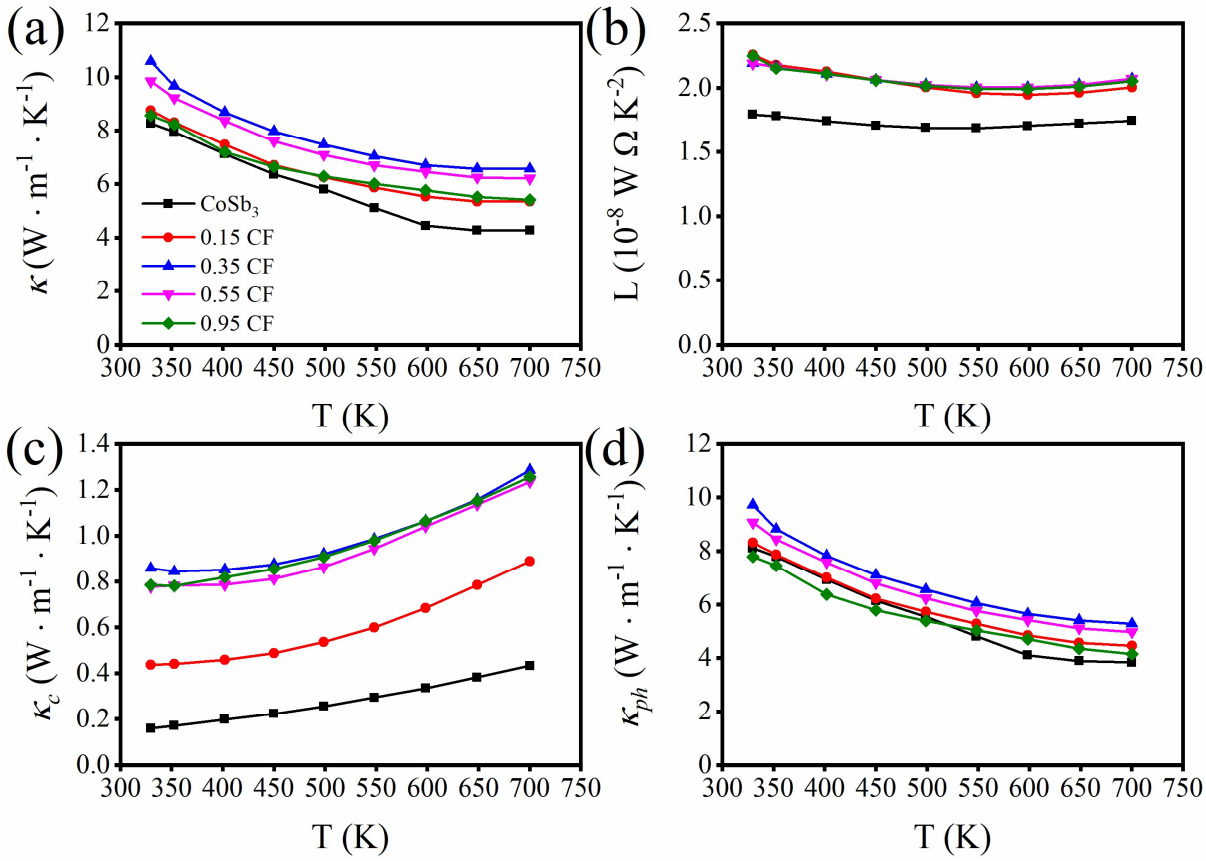

Fig 13 Temperature dependence of thermal transport properties of $CoSb_3$- xwt% CF (x=0, 0.15, 0.35, 0.55 and 0.95) composites (a) Total thermal conductivity (κ), (b) The calculated Lorenz number (L), (c) carrier thermal conductivity (κ_C), and (d) Phonon thermal conductivity κ_{ph}.

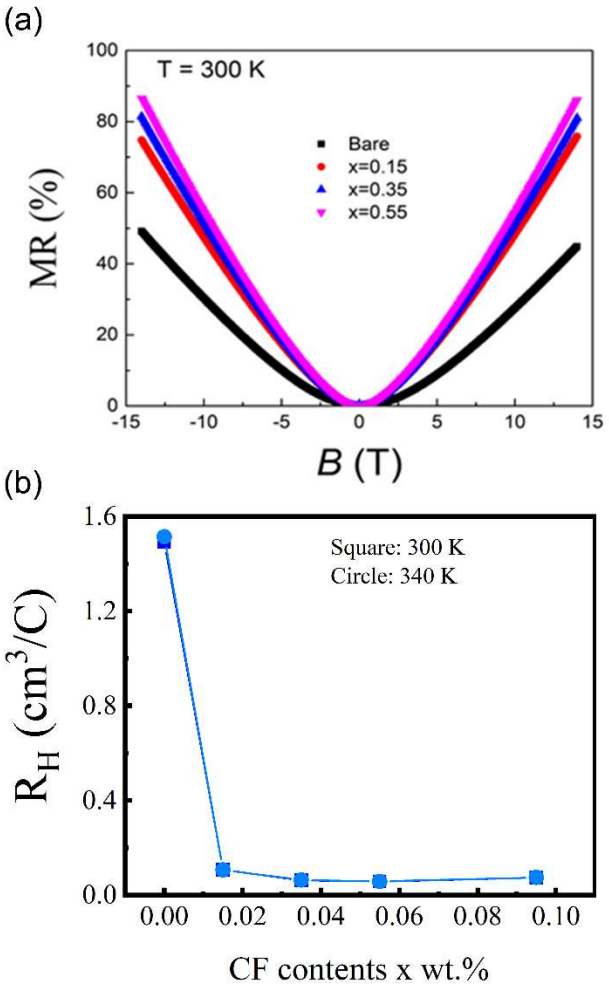

Fig 14 Magnetoresistance (MR) (a), and Hall effect (b), at room temperature of pure and carbon fiber incorporated $CoSb_3$ samples.

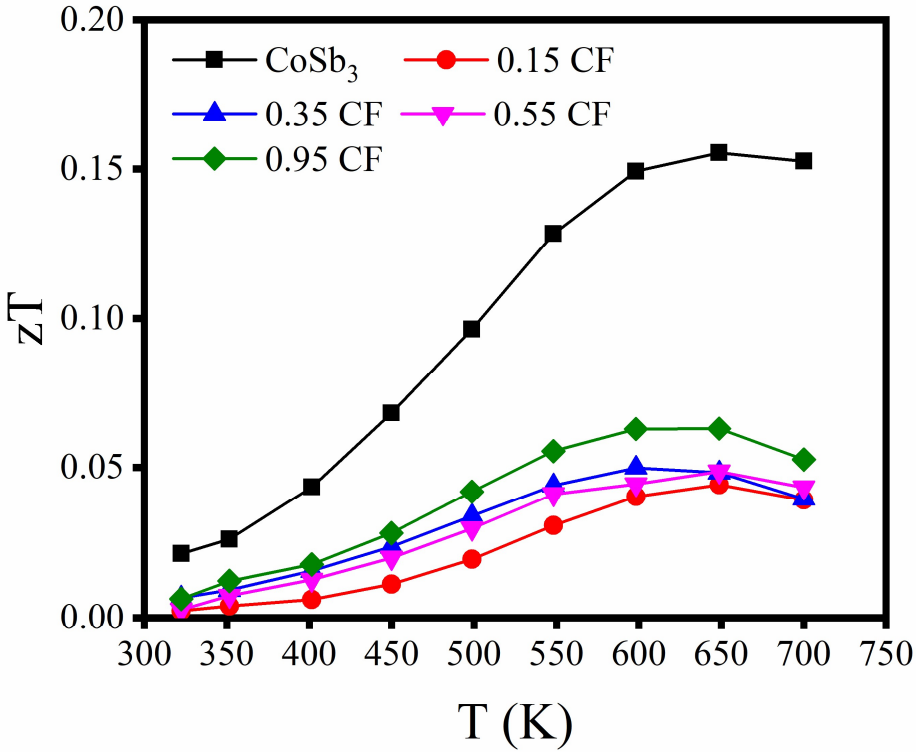

Fig 15 Temperature dependence of figure of merit (zT) of pure $CoSb_3$ and CF incorporated $CoSb_3$ samples ($CoSb_3$-xwt% CF (x =0, 0.15, 0.35, 0.55 and 0.95wt.% carbon fiber).